Nano Research

Open Access

Research Article

Synergy of nickel based single atom and nanoparticle for photothermal hydrogen production from non-food-feed fermentation broth

Jiaqi Pang[1,§], Yongying Sang[1,§], Tianci Chang[1,§], Dachao Yuan[1,2] ✉, Guanda Han[1], Luping Ma[1], Shuhua Yang[1], Yaguang Li[1,2] ✉, and Jinhua Ye[2,3,4] ✉

[1] *College of Mechanical and Electrical Engineering, Technology Innovation Center of Intelligent Agricultural Equipment, Hebei Agricultural University, Baoding 071001, China*
[2] *Research Center for Solar Driven Carbon Neutrality, The College of Physics Science and Technology, Institute of Life Science and Green Development, Hebei University, Baoding 071002, China*
[3] *Advanced Catalytic Materials Research Center, School of Materials Science and Engineering, Tianjin University, Tianjin 300072, China*
[4] *International Center for Materials Nanoarchitectonics (WPI-MANA), National Institute for Materials Science (NIMS), 1-1 Namiki, Tsukuba, Ibaraki 305-0044, Japan*
§ *Jiaqi Pang, Yongying Sang, and Tianci Chang contributed equally to this work.*

Cite this article: *Nano Research*, **2026**, *19*, 94908665. https://doi.org/10.26599/NR.2026.94908665

ABSTRACT: Catalytic hydrogen generation from non-food-feed biomass is pivotal for carbon-neutral economy, which is limited by low hydrogen productivity, high CO concentration, and excessive fossil energy consumption. Herein, we demonstrate a synergistic effect between Ni^{2+} single atoms and metallic Ni nanoparticles supported on $La_2O_2CO_3$ ($Ni_{SA+NP}/La_2O_2CO_3$), which attains a fermentation broth reforming with a stable hydrogen production rate of 2373 $mmol \cdot g^{-1} \cdot h^{-1}$ and ~ 99.6% hydrogen purity at 550 °C, notably higher than the counterparts. Theoretical calculations reveal that the multiscale effect of Ni^{2+} single atoms and metallic Ni nanoparticles can promote the dissociation of C–C/C–H bonds to enhance the organics decomposition and strengthen the CO adsorption as well as water gas shift reaction to reduce the CO concentration in hydrogen gas. Combined with photothermal reactor, the natural sunlight driven photothermal fermentation broth reforming over $Ni_{SA+NP}/La_2O_2CO_3$ achieves 1129 $mmol \cdot g^{-1} \cdot h^{-1}$ of hydrogen evolution rate, > 99.6% hydrogen purity and an enthalpy change solar-to-hydrogen efficiency of 16.6%, that outperforms the 10% commercial utilization target set by the US Department of Energy. This work offers a novel perspective for the development of sunlight driven fermentation broth reforming through the ingenious design of synergistic catalytic sites.

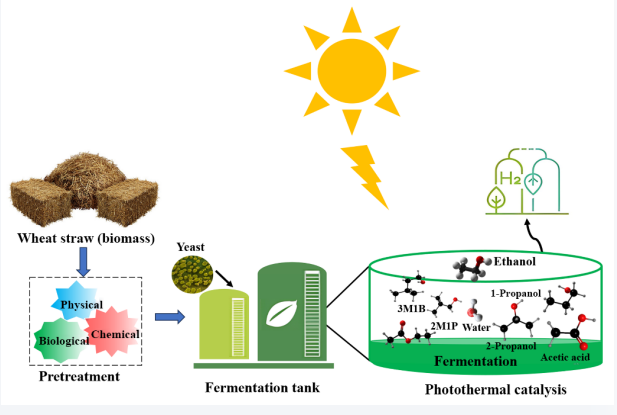

KEYWORDS: photothermal catalysis, hydrogen, fermentation broth, synergistic effect, nickel

1 Introduction

Catalytic hydrogen (H_2) generation from biomass has emerged as a clean energy carrier to drive a carbon-neutral economy in the post-fossil era [1, 2]. Compared to food-feed biomass, such as corn, the fermentation broth obtained from lignocellulose is one of the most promising candidates for hydrogen production [3, 4]. Given that the water content of lignocellulose derived fermentation broth exceeds 92%, reforming process can effectively convert the ethanol and other hydrocarbon substances in fermentation broth into H_2 [3–6]. However, due to the high moisture content, the energy consumption for producing 1 ton of H_2 from lignocellulose derived fermentation broth is as high as 35 GJ, equivalent to the combustion of 1.5 tons of coal [3]. Therefore, it is imperative to reduce the fossil energy consumption of H_2 produced from lignocellulose derived fermentation broth. To overcome this

Received: December 31, 2025; **Revised:** February 23, 2026
Accepted: March 23, 2026

✉Address correspondence to Dachao Yuan, jdydch@hebau.edu.cn; Yaguang Li, liyaguang@hbu.edu.cn; Jinhua Ye, Jinhua.ye@hbu.edu.cn

challenge, photothermal catalysis can be employed [7–10], which has the potential to drive H_2 production from fermentation broth with zero secondary energy input.

Catalysts are the key factor affecting H_2 production and in view of the main hydrocarbon component in fermentation broth is ethanol, we need to draw on the catalysts for ethanol reforming. Considering the economic feasibility, Ni-based catalysts are the most widely used non-noble catalysts for ethanol steam reforming. To further increase the hydrogen production activity, scientists mainly use alloying strategy to adjust the dissociated ability for the C–C bonds and C–H bonds in ethanol. For example, Yu et al synthesized Cu_1Ni_9 nanoalloy to showcase a H_2 production rate of 1785 mmol·g^{-1}·h^{-1} at 550 °C [11], created the highest activity of Ni based catalysts. However, the addition of heterogeneous metals will reduce the CO adsorption and activation ability of Ni, resulting in ~ 4% content of CO in the H_2, reducing the applicability [3, 12, 13].

Herein, we constructed lanthanum oxycarbonate species ($La_2O_2CO_3$) supported Ni^{2+} single atoms and metallic Ni nanoparticles ($Ni_{SA+NP}/La_2O_2CO_3$). For the reforming of lignocellulose derived fermentation broth, the $Ni_{SA+NP}/La_2O_2CO_3$ attains a thermocatalytic hydrogen production rate of 2373 mmol·g^{-1}·h^{-1} at 550 °C with 72 h stability, which is not only notably higher than those of Ni single atoms and Ni nanoparticles but also superior to the record value for H_2 production through pure bioethanol reforming (~ 1800 mmol·g^{-1}·h^{-1} at 550 °C) [14]. Moreover, the CO content of H_2 produced over $Ni_{SA+NP}/La_2O_2CO_3$ is as low as ~ 0.4%, significantly lower than the ~ 4% content achieved from other catalysts. Theoretical calculations show that the multiscale effect between Ni^{2+} single atoms and metallic Ni nanoparticles not only activates C–H and C–C bonds, but also enhances CO adsorption, leading to a coupling of enhanced H_2 production and reduced CO content. After coupling of a self-developed photothermal reactor, the $Ni_{SA+NP}/La_2O_2CO_3$ can achieve a H_2 yield of 1129 mmol·g^{-1}·h^{-1} and an enthalpy change solar-to-hydrogen (STH) conversion efficiency of 16.6%, under 1.3 kW·m^{-2} of sunlight irradiation. This work reveals that the synergistic of Ni single atoms and Ni nanoparticles paves a novel pathway for producing high quality hydrogen directly from fermentation broth, which is an innovative solution for the practical application of sunlight-driven biological hydrogen production technology.

2 Results and discussion

2.1 Ni single-atoms/nanoparticles synergistic catalyst

The synergistic Ni single atoms and nanoparticles co-existed catalyst ($Ni_{SA+NP}/La_2O_2CO_3$) was synthesized by using the joint of sol–gel and precipitation method. Firstly, nickel salt and lanthanum salt were mixed with an explosive (ammonium nitrate) to form a homogeneous gel. Upon annealing, high temperatures were generated to obtain Ni single atoms loaded on $La_2O_2CO_3$ ($Ni_{SA}/La_2O_2CO_3$). The inductively coupled plasma-optical emission spectroscopy (ICP-OES) tested Ni/La ratio of $Ni_{SA}/La_2O_2CO_3$ is 2.8/97.2 (Table S1 in the ESM). X-ray diffraction (XRD) pattern of $Ni_{SA}/La_2O_2CO_3$ was similar to the characteristic diffraction peaks of pure $La_2O_2CO_3$ (Fig. S1 in the ESM) [15, 16], and the transmission electron microscopy (TEM) image of $Ni_{SA}/La_2O_2CO_3$ presents a nanosheet morphology (Fig. 1(a)). The elemental mapping images demonstrate that Ni, La, O, and C exhibit homogeneous distribution on the surface of $Ni_{SA}/La_2O_2CO_3$ (Fig. 1(b)). High-angle annular dark-field scanning transmission electron microscopy (HAADF-STEM) measurement was used to characterize the Ni species in $Ni_{SA}/La_2O_2CO_3$ and the atomic level isolated bright dots (orange circle highlighted) are observed in Fig. 1(c), indicating high dispersion of Ni species. X-ray absorption near edge structure (XANES) and extended X-ray absorption fine-structure (EXAFS) spectroscopy were performed to reveal the coordination environment of Ni in $Ni_{SA}/La_2O_2CO_3$. The Ni K-edge XANES spectrum of $Ni_{SA}/La_2O_2CO_3$ with a higher energy value than that of Ni foil and similar to NiO confirms the oxidation state of Ni species [17], corresponding to the X-ray photoelectron spectroscopy (XPS) result (Fig. S2 in the ESM). It indicates that the Ni species in $Ni_{SA}/La_2O_2CO_3$ maintain +2 valence state, even after hydrogen reduction. Fourier transformed (FT) EXAFS spectrum of $Ni_{SA}/La_2O_2CO_3$ shows a single Ni–O scattering peak at 1.0–2.0 Å (Fig. 1(e)), which confirms the single-atom state of Ni species in $Ni_{SA}/La_2O_2CO_3$ [18, 19]. The quantitative EXAFS fitting was performed to extract the structural parameters (Fig. S3 in the ESM). The fitted results reveal that the coordination number for $Ni_{SA}/La_2O_2CO_3$ is 5.16, with a Ni–O bond distance of 1.87 Å (Table S2 in the ESM). Then, the $Ni_{SA}/La_2O_2CO_3$ was immersed in a nickel nitrate solution, and NiO nanoparticles were precipitatied on the surface of $Ni_{SA}/La_2O_2CO_3$ by titrating ammonia. Finally, the sample was reduced by hydrogen to form $Ni_{SA+NP}/La_2O_2CO_3$. The Ni/La ratio of $Ni_{SA+NP}/La_2O_2CO_3$ is 5.9/94.1 (Table S1 in the ESM). TEM image shows that the nanoparticles (circled in yellow color) with ca. ~ 8 nm are dispersed on $Ni_{SA+NP}/La_2O_2CO_3$ (Fig. 1(f)). After hydrogen reduction, the measured lattice stripe is 0.201 nm, corresponding to the lattice spacing of Ni(111) crystal plane, accompanied by the atomic level bright spots (Fig. 1(g)). XRD cannot detect the crystal structure of Ni species in $Ni_{SA+NP}/La_2O_2CO_3$ (Fig. S4 in the ESM) [15, 16], while the Raman spectroscopy (Fig. S5 in the ESM) confirms the existence of Ni–O bond and CO_3 [20]. Moreover, XPS verifies the coexistence of Ni^{2+} and Ni^0 in $Ni_{SA+NP}/La_2O_2CO_3$ (Fig. S6 in the ESM) [21, 22]. We further used X-ray absorption structure to analyze the fine structure of Ni in $Ni_{SA+NP}/La_2O_2CO_3$ (Fig. S7(a) in the ESM). The FTEXAFS spectrum of $Ni_{SA+NP}/La_2O_2CO_3$ shows the Ni–O bond at 1.0–2.0 Å and metallic Ni–Ni bond at 2.0–2.5 Å (Fig. S7(b) in the ESM), accompanied by the lacking of Ni–O–Ni bond at 2.5–3.0 Å (Fig. S7(b) in the ESM). Therefore, we have clearly prepared $Ni_{SA+NP}/La_2O_2CO_3$ containing Ni^{2+} single atoms and metallic Ni nanoparticles supported on $La_2O_2CO_3$ nanosheets as shown in Fig. 1(h). The specific surface area of $Ni_{SA+NP}/La_2O_2CO_3$ was calculated to be 46.1 m^2·g^{-1} (Fig. S8 in the ESM), slightly lower than that of $Ni_{SA}/La_2O_2CO_3$ and $Ni_{NP}/La_2O_2CO_3$ with same Ni content.

2.2 The fermentation broth reforming of $Ni_{SA+NP}/La_2O_2CO_3$

We used wheat straw to make the fermentation broth, which contains ~ 93% H_2O, ~ 6.8% ethanol, ~ 0.6% acetic acid, trace amount of propanol, 2-methy-1-propanol, 3-methy-1-butanol, ethyl acetate, etc. [3, 5, 6], as shown in Table S3 in the ESM. The $Ni_{SA+NP}/La_2O_2CO_3$, $Ni_{SA}/La_2O_2CO_3$, $Ni_{NP}/La_2O_2CO_3$ (Fig. S9 in the ESM), and $La_2O_2CO_3$ nanosheets (Fig. S10 in the ESM) were used to verify the role of the Ni single atoms and Ni nanoparticles in the hydrogen production from fermentation broth. Figure 2(a) shows the hydrogen production rates of these four catalysts depend on the temperature range of 200 to 700 °C. $Ni_{SA+NP}/La_2O_2CO_3$ exhibits the highest activity with a hydrogen production rate of 2373 mmol·g^{-1}·h^{-1} at 550 °C (Fig. 2(a)). This rate is approximately

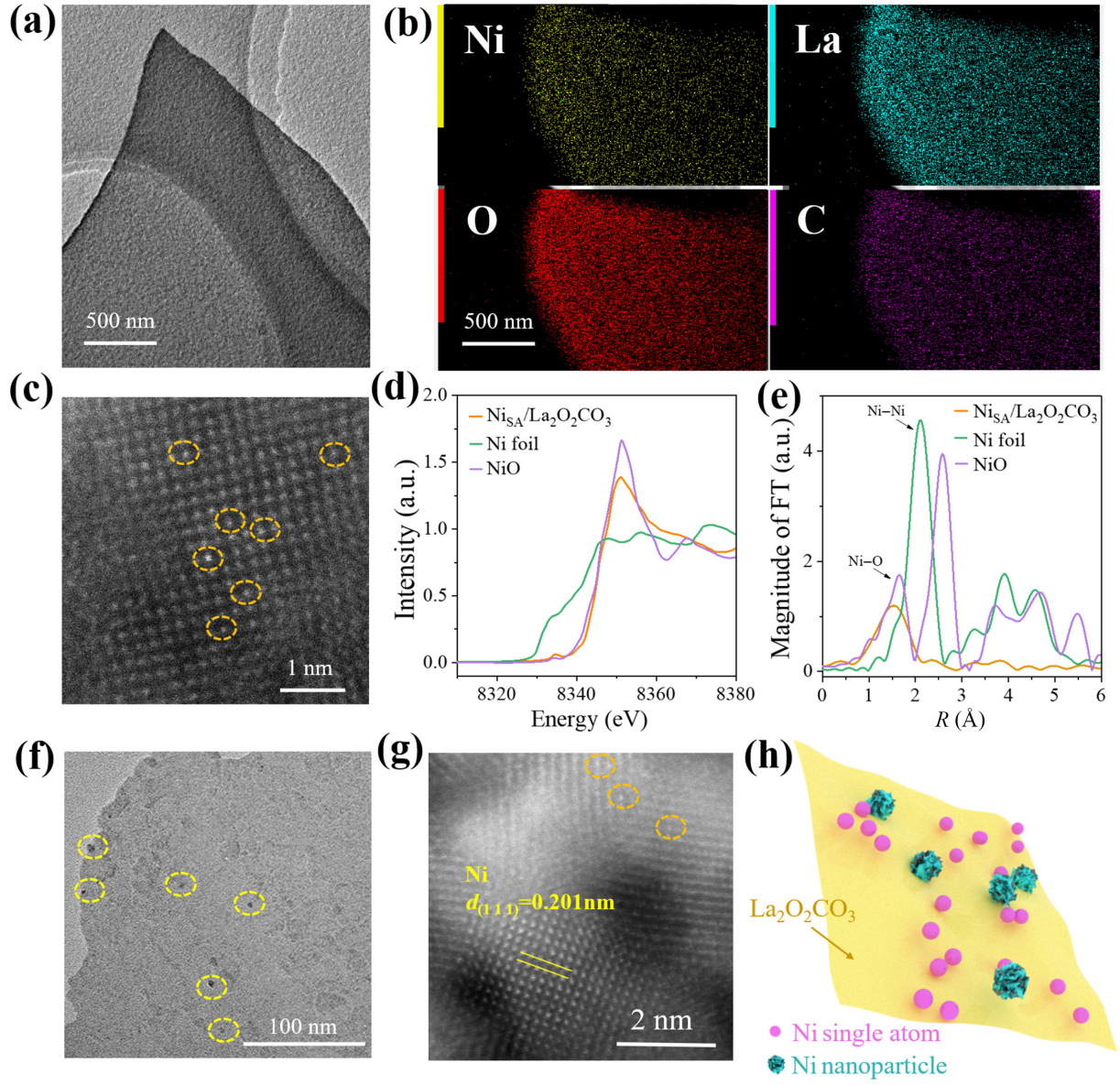

Figure 1 The structure of $Ni_{SA+NP}/La_2O_2CO_3$. (a) TEM image, (b) EDS mapping, (c) aberration corrected STEM image of $Ni_{SA}/La_2O_2CO_3$. (d) XANES spectra at the Ni K-edge for $Ni_{SA}/La_2O_2CO_3$, Ni foil, and NiO. (e) EXAFS curves of $Ni_{SA}/La_2O_2CO_3$, Ni foil, and NiO. (f) TEM image, (g) HRTEM image, (h) schematic diagram of $Ni_{SA+NP}/La_2O_2CO_3$. The yellow sheet represents $La_2O_2CO_3$, the purple spheres denote Ni single atoms, and the green clusters stand for Ni NPs.

4.3 times higher than that of $Ni_{SA}/La_2O_2CO_3$ (539 mmol·g^{-1}·h^{-1}) and 10.4 times higher than that of $Ni_{NP}/La_2O_2CO_3$ (221 mmol·g^{-1}·h^{-1}). Bare $La_2O_2CO_3$ nanosheets exhibit weak activity and it reveals that the hydrogen produced activity is originated from the nickel species. When the temperature exceeds 550 °C, the hydrogen production performance decreases because the water gas shift reaction is inhibited at high temperatures. Since thermocatalytic real fermentation broth reforming is rarely investigated and the main hydrocarbon substance in fermentation broth is ethanol, Fig. 2(b) presents the comparison of hydrogen production performance of $Ni_{SA+NP}/La_2O_2CO_3$ with the advanced catalysts for pure bioethanol steam reforming at 550 °C. It is verified that the hydrogen production rate of $Ni_{SA+NP}/La_2O_2CO_3$ is nearly 1.3 times higher than that of the reported best catalysts, such as La-950 (1824 mmol·g^{-1}·h^{-1}) [14], Cu_1Ni_9/YSZ (1785 mmol·g^{-1}·h^{-1}) [11], Cu-Ni/SiO_2 (617.4 mmol·g^{-1}·h^{-1}) [23], and others. Based on the ICP-OES result (Table S1 in the ESM) and assuming all Ni atoms participated in H_2 generation, the H_2 generation turnover frequency (TOF) of $Ni_{SA+NP}/La_2O_2CO_3$, $Ni_{SA}/La_2O_2CO_3$, and $Ni_{NP}/La_2O_2CO_3$ is 1.71, 3.47, 0.54 S^{-1} at 550 °C, respectively (Fig. S11 in the ESM). Evidently, it is shown that the synergistic of single atoms and nanoparticles can effectively improve the hydrogen production performance of nickel-based materials from lignocellulose derived fermentation broth. We also tested the hydrogen production performance of typical organics in fermentation broth (ethanol, acetic acid, propanol, 3-methy-1-butanol, 2-methy-1-propanol, and ethyl acetate) and Fig. S12 in the ESM showed that $Ni_{SA+NP}/La_2O_2CO_3$ exhibits the highest activity for all components. In addition to the high activity, the hydrogen generation rate of $Ni_{SA+NP}/La_2O_2CO_3$ fluctuated from 2132 to 2466 mmol·g^{-1}·h^{-1} during a 72-hour successive test at 550 °C (Fig. 2(c)). No significant shifts in the binding energies of Ni 2p, La 3d, C 1s, and O 1s were observed in the XPS spectra of $Ni_{SA+NP}/La_2O_2CO_3$ after stability test (Fig. S13 in the ESM). Furthermore, post-reaction XRD pattern and

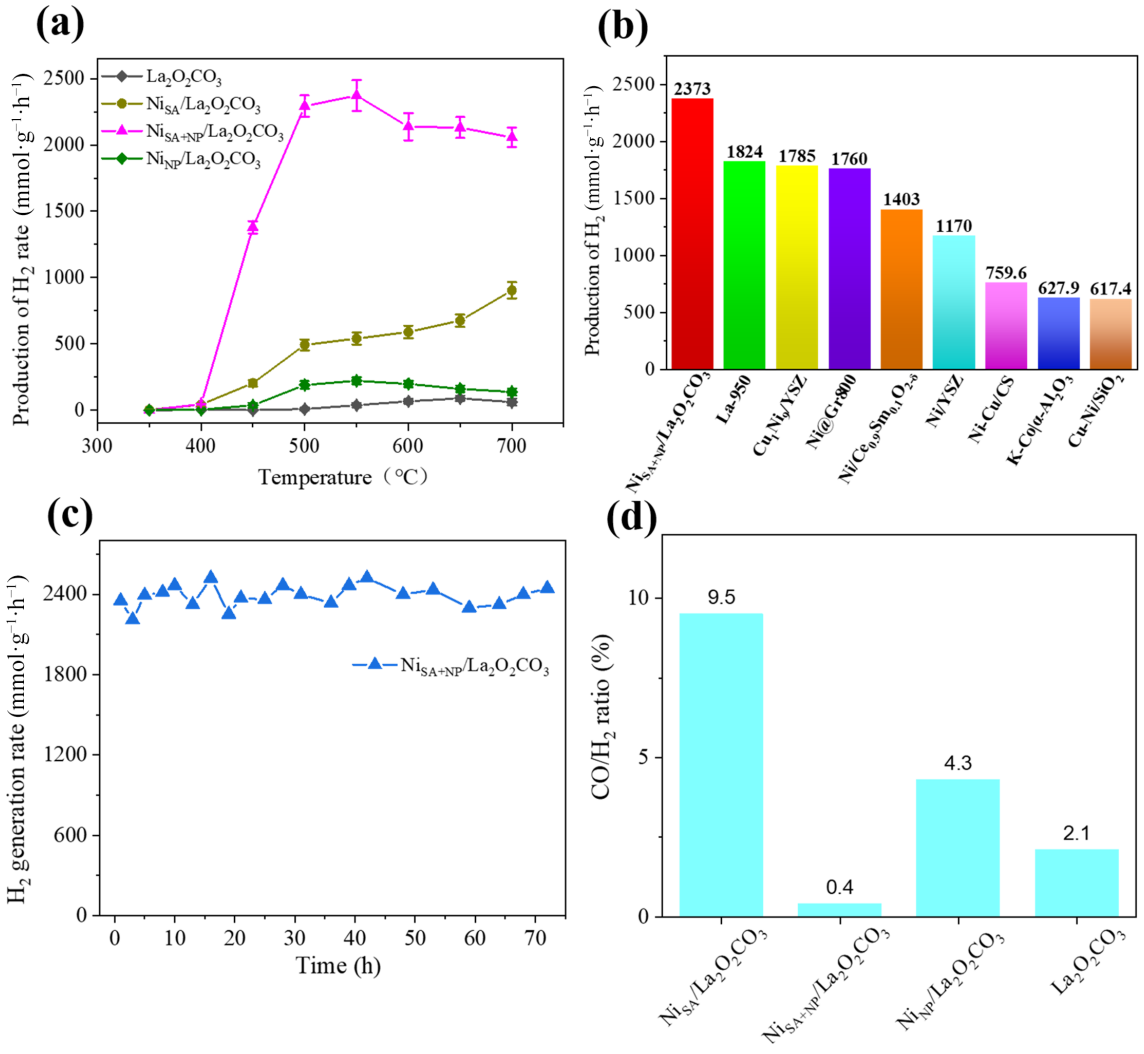

Figure 2 The performance of catalysts for fermentation broth reforming to H_2. (a) The H_2 generation rate of thermocatalytic fermentation broth reforming over different catalysts. (b) The H_2 generation performance comparison between $Ni_{SA+NP}/La_2O_2CO_3$ and reported advanced non-noble, noble metal catalysts from ethanol steam reforming. (c) The stability test of $Ni_{SA+NP}/La_2O_2CO_3$ for fermentation broth reforming at 550 °C for 72 h. (d) The CO/H_2 ratio of the gas produced from fermentation broth reforming over different catalysts.

TEM characterization of $Ni_{SA+NP}/La_2O_2CO_3$ confirmed that the catalyst's phase composition and morphological structure remained unaltered after stability test, which further verifies the excellent chemical and structural stability of the $Ni_{SA+NP}/La_2O_2CO_3$ catalyst (Fig. S14 in the ESM). Another striking achievement lies in CO mitigation (Fig. 2(d)). The CO/H_2 ratio of produced hydrogen over $Ni_{SA+NP}/La_2O_2CO_3$ is only 0.4%, which is orders of magnitude lower than $Ni_{SA}/La_2O_2CO_3$ (9.5%), $Ni_{NP}/La_2O_2CO_3$ (4.3%), and even lower than pure $La_2O_2CO_3$ (2.1%) shown in Fig. S15 in the ESM. To the best of our knowledge, this is the lowest CO content ever reported for the hydrogen produced from fermentation broth, significantly reducing the need for additional CO purification steps. Therefore, the $Ni_{SA+NP}/La_2O_2CO_3$ combines high H_2 productivity, long-term stability, and unprecedentedly low CO emissions, addressing a core bottleneck in fermentation broth-to-hydrogen conversion.

2.3 The synergistic mechanism of Ni single atoms and nanoparticles

To investigate the performance of Ni-based catalysts supported on $La_2O_2CO_3$ for the hydrogen production from fermentation broth, a combination of *in-situ* characterization and theoretical calculations was employed. Figure 3(a) presents the *in-situ* diffuse reflectance infrared Fourier transform spectra (DRIFTS) of the $Ni_{SA+NP}/La_2O_2CO_3$ during fermentation broth-to-hydrogen conversion, recorded across temperatures from 25 to 400 °C. At room temperature (25 °C), the peak at 2977 cm^{-1} assigned to the C–H stretching in ethanol [24], indicating the adsorption of ethanol on catalysts. The peak at 1758 cm^{-1} corresponds to C=O in acetaldehyde (CH_3CHO) and it indicates that ethanol is decomposed via acetaldehyde route [25]. The CO_2-related peaks (2310 and 2362 cm^{-1}) strengthen along with the increase of temperature [24]. The rising of temperature leads to an increase in CO_2 content associated with hydrogen production from the fermentation broth, resulting in an enhancement of the adsorption peaks. In the DRIFTS of $Ni_{NP}/La_2O_2CO_3$ and $Ni_{SA}/La_2O_2CO_3$, the adsorption peak of CO at 2162 cm^{-1} is particularly prominent (Fig. S16 in the ESM), while the chemisorbed CO signal is almost disappeared in the DRIFTS over $Ni_{SA+NP}/La_2O_2CO_3$ (Fig. 3(a)). To further verify this phenomenon, we conducted CO temperature-programmed desorption (CO-TPD) experiments. Figure 3(b)

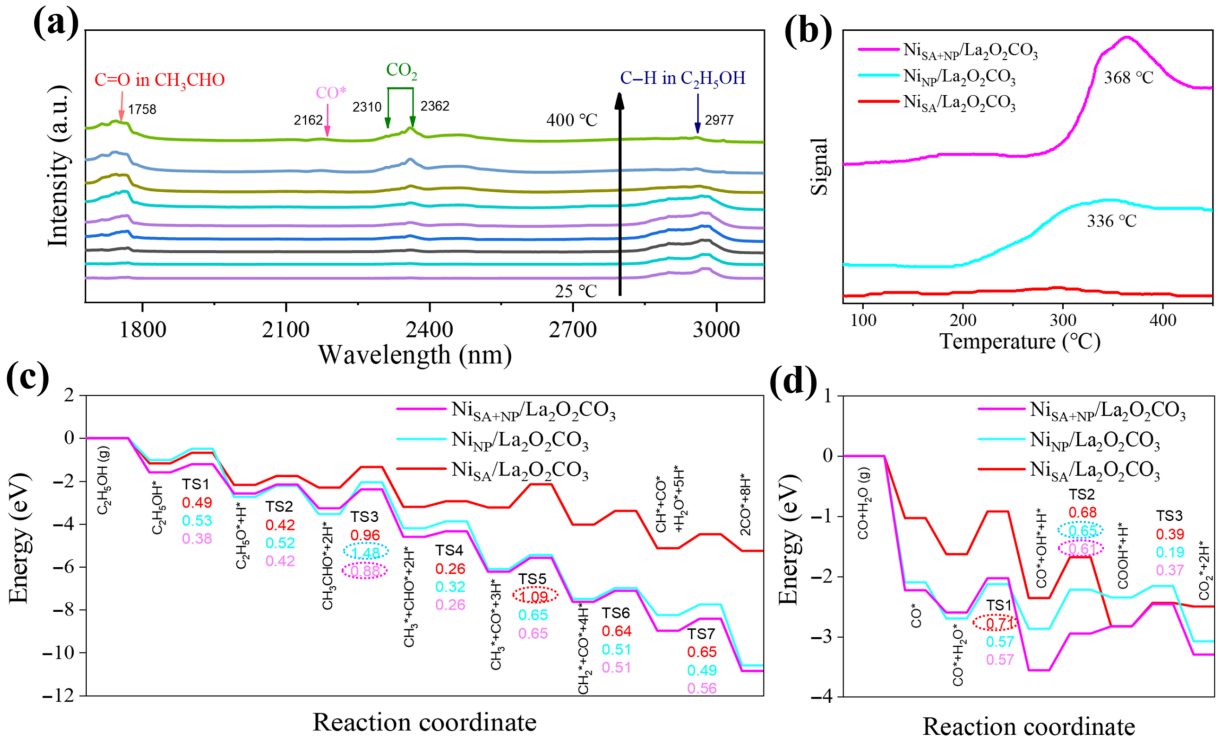

Figure 3 Reaction mechanism of ethanol steam reforming and water gas shift reaction. (a) *In-situ* DRIFTS obtained for $Ni_{SA+NP}/La_2O_2CO_3$ under fermentation broth reforming condition. (b) CO TPD curves over different catalysts. (c) Potential energy diagram of ethanol decomposition over different catalysts, including ZPE correction energy, X* denotes the adsorbed substance. (d) Potential energy diagram of reaction for CO and H_2O over different catalysts, including ZPE correction energy, X* denotes the adsorbed substance.

depicts CO-TPD profiles of three catalysts and the CO desorption peak temperatures over $Ni_{SA+NP}/La_2O_2CO_3$, $Ni_{NP}/La_2O_2CO_3$, $Ni_{SA}/La_2O_2CO_3$ are 368, 336 °C, and no distinct desorption signal, respectively. Therefore, the $Ni_{SA+NP}/La_2O_2CO_3$ has the highest CO adsorption energy among the three catalysts and the weak CO adsorption peak in DRIFTS over $Ni_{SA+NP}/La_2O_2CO_3$ should be caused by the particularly low CO content in the atmosphere.

Since the main hydrocarbon substance in fermentation broth is ethanol and ethanol contains the typical robust C–C, C–H bonds, Fig. 3(c) displays the reaction energy profiles of ethanol steam reforming over the three catalysts (Fig. S17 in the ESM). The reaction coordinate starts with ethanol, which was firstly dehydrogenated as CH_3CHO. Subsequent step involves C–C bond cleavage to form CH_3 and CHO intermediates, which is the rate determining step for $Ni_{SA+NP}/La_2O_2CO_3$ (0.88 eV) and the $Ni_{NP}/La_2O_2CO_3$ (1.48 eV). The Bader charge of Ni single atoms on $La_2O_2CO_3$ is +1.31 |e| and it indicates that Ni single atoms can form strong electrostatic adsorption with oxygen ion in CH_3CHO (Fig. S18 in the ESM). While the Bader charge of Ni in Ni nanoparticle is +0.12 |e|. It suggests that Ni in Ni nanoparticle is electron rich and can interact well with the CH_3 in CH_3CHO (Fig. S19 in the ESM). Therefore, the coupling of Ni single atoms and Ni nanoparticles can strongly adsorb CHO and CH_3 of CH_3CHO, respectively, promoting the dissociation of C–C bond. For $Ni_{SA}/La_2O_2CO_3$, the CH_3 decomposed as CH_2 is the rate determining step (1.09 eV) and it reveals that Ni single toms are not active for C–H cleavage. Therefore, $Ni_{SA+NP}/La_2O_2CO_3$ exhibits the lowest overall energy barriers (0.88 eV for TS3), in comparison with $Ni_{SA}/La_2O_2CO_3$ and $Ni_{NP}/La_2O_2CO_3$. It reveals that the dual-site catalyst enhances the ability to activate ethanol decomposition.

The water gas shift (WGS) reaction ($CO + H_2O \rightarrow CO_2 + H_2$) is critical for upgrading H_2 yield, and its energy profile (Fig. 3(d)) reveals key differences between catalysts. The adsorption energy of CO on $Ni_{SA+NP}/La_2O_2CO_3$, $Ni_{NP}/La_2O_2CO_3$, $Ni_{SA}/La_2O_2CO_3$ is 2.23, 2.1, 1.03 eV, respectively, corresponding to the CO TPD results (Fig. 3(b)). The atomic structures reveal that the Ni single atoms and Ni nanoparticles adsorb oxygen and carbon separately from CO (Fig. S19 in the ESM), thereby enhancing the adsorption capacity of CO. Further, the rate determining step's energy barrier for $Ni_{SA+NP}/La_2O_2CO_3$, $Ni_{NP}/La_2O_2CO_3$, $Ni_{SA}/La_2O_2CO_3$ is 0.61, 0.65, 0.71 eV, respectively. Therefore, we infer that $Ni_{SA+NP}/La_2O_2CO_3$ has both strong CO adsorption ability and superior WGS activity, which promotes the WGS reaction of CO and leads to low CO concentration in hydrogen gas.

2.4 The photothermal fermentation broth reforming over $Ni_{SA+NP}/La_2O_2CO_3$

Photothermal technology exploits photon–phonon interactions to transfer energy, demonstrating significant potential in hydrogen generation [26, 27]. Based on the outstanding thermocatalytic performance of the $Ni_{SA+NP}/La_2O_2CO_3$, the catalyst was further employed for photothermal fermentation broth-to-hydrogen conversion (Fig. S20 in the ESM). Based on the photothermal catalytic system, Fig. 4(a) outlines our designed system to convert agricultural and forestry waste as hydrogen without secondary energy. Firstly, the wheat straw—a representative lignocellulosic biomass rich in cellulose and hemicellulose—is fed into a fermentation tank, where yeast mediates the breakdown of complex carbohydrates into a mixed fermentation broth, containing water, ethanol and trace amount of acetic acid, 1-propanol, etc. Subsequently, the fermentation broth is introduced into a

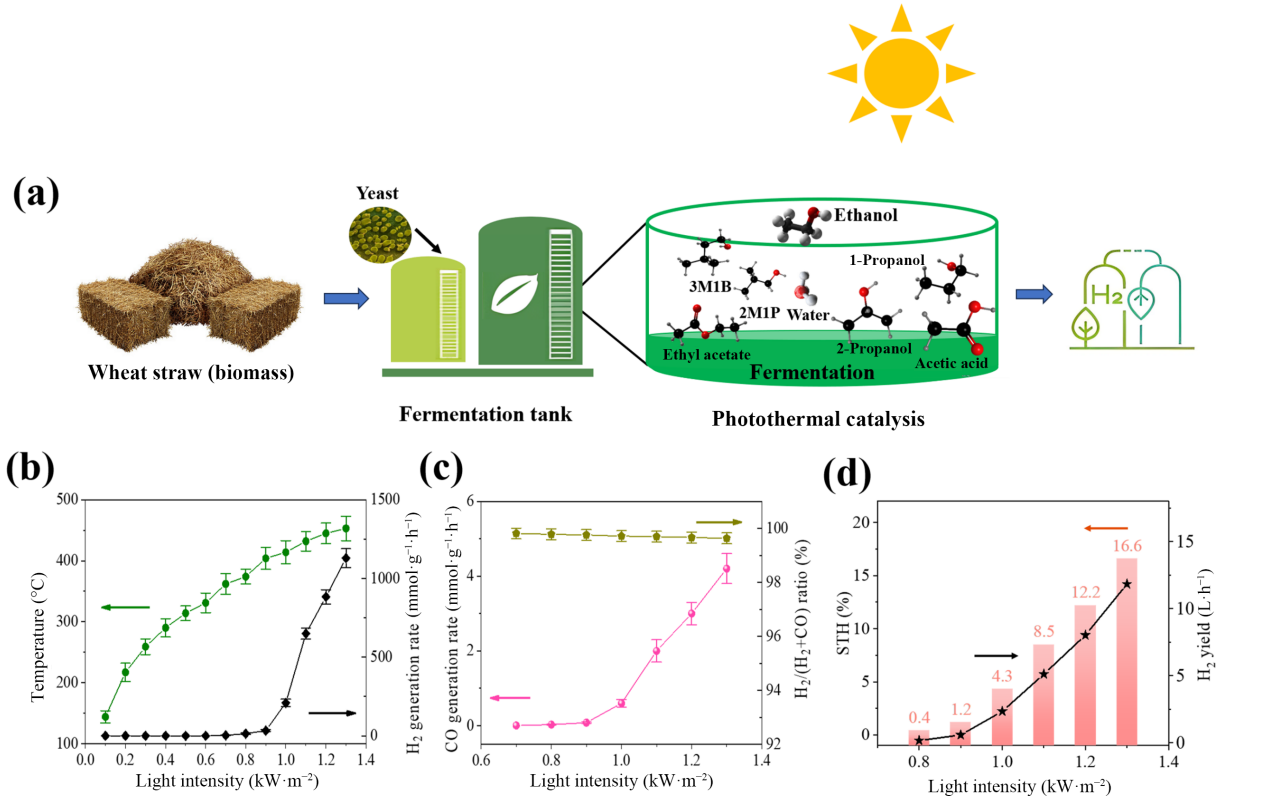

Figure 4 The photothermal fermentation broth reforming. (a) The sketch map of secondary energy free system to convert agricultural and forestry waste as hydrogen. (b) The temperatures and photothermal fermentation broth reforming performance of $Ni_{SA+NP}/La_2O_2CO_3$ under various sunlight irradiation. (c) The corresponding CO generation rate and $H_2/(H_2+CO)$ ratio over $Ni_{SA+NP}/La_2O_2CO_3$ under various sunlight irradiations. (d) The scalable photothermal fermentation broth reforming performance with STH over $Ni_{SA+NP}/La_2O_2CO_3$ under various sunlight irradiations.

$Ni_{SA+NP}/La_2O_2CO_3$ assisted photothermal catalytic reactor, in which the organic components in the broth undergo catalytic conversion to produce H_2, and it requires the photothermal catalytic system to be able to operate under weak sunlight irradiation. Figure 4(b) quantifies the system's photothermal heating capability under weak sunlight irradiation (0–1.3 kW·m^{-2}). As light intensity increases, the reactor temperature rises monotonically: from ~ 250 °C at 0.4 kW·m^{-2} of sunlight irradiation to over 450 °C at 1.3 kW·m^{-2} (1.3 suns) of sunlight irradiation. This steep elevation confirms efficient conversion of light energy to thermal energy, which supplies the activation energy required for catalytic reactions in the broth. The photothermal fermentation broth reforming over $Ni_{SA+NP}/La_2O_2CO_3$ shows a H_2 generation rate of 209 mmol·g^{-1}·h^{-1} under 1 sun irradiation (Fig. 4(a)). Further, the H_2 production rate sharply increases to 1129 mmol·g^{-1}·h^{-1} under 1.3 suns irradiation, which is nearly 1.1 times higher than that of the reported best catalysts in > 3 suns driven ethanol steam reforming, such as SA Fe-CeO_2/Ti (984 mmol·g^{-1}·h^{-1}) [9], Ni SA/CeO_2 (519 mmol·g^{-1}·h^{-1}) [8], 0.04Ni/Cu (176.6 mmol·g^{-1}·h^{-1}) [28], PdPSA-CdS (35.1 mmol·g^{-1}·h^{-1}) [29], Au/TiO_2 (5.6 mmol·g^{-1}·h^{-1}) [30], and others as listed in Table S4 in the ESM. Obviously, it is demonstrated that the synergistic of $Ni_{SA+NP}/La_2O_2CO_3$ and photothermal device is the most active system in sunlight driven hydrogen production from fermentation broth to date. Figure 4(c) shows the byproduct CO in H_2 is increased with promoting the light intensity and highest generation rate is ~ 4 mmol·g^{-1}·h^{-1}. The $H_2/(CO+H_2)$ ratio of produced hydrogen over $Ni_{SA+NP}/La_2O_2CO_3$ is totally higher than 99.6%, ensuring the high purity of hydrogen gas. Since the $Ni_{SA+NP}/La_2O_2CO_3$ can be scalably produced (Fig. S21 in the ESM), 40 g of $Ni_{SA+NP}/La_2O_2CO_3$ is applied for the laboratory scalable photothermal fermentation broth reforming. As the sunlight density increases to 1 sun, $Ni_{SA+NP}/La_2O_2CO_3$ achieves 2.35 L·h^{-1} hydrogen production rate (Fig. 4(d)). With the light intensity increased to 1.3 suns, the H_2 yield can reach to 11.83 L·h^{-1} (Fig. 4(d)). Therefore, the combine of $Ni_{SA+NP}/La_2O_2CO_3$ and photothermal device presents an efficient approach for sunlight driven bio-hydrogen production. According to the experimental data, Fig. 4(d) shows that the enthalpy change STH conversion efficiency of this demonstration reaches 16.6% under 1.3 suns illumination (details shown in Experimental section in the ESM), that outperforms the 10% commercial utilization target set by the US Department of Energy [31–33].

3 Conclusions

In this work, we fabricated a synergistic catalyst ($Ni_{SA+NP}/La_2O_2CO_3$) with Ni single atoms and nanoparticles supported on $La_2O_2CO_3$, which realizes a remarkable hydrogen production activity from fermentation broth. Thermal catalysis experiments verified that the $Ni_{SA+NP}/La_2O_2CO_3$ catalyst manifested an outstandingly high hydrogen production rate of 2373 mmol·g^{-1}·h^{-1} at 550 °C with 0.4% CO content, which is much higher than that of $Ni_{SA}/La_2O_2CO_3$ (539 mmol·g^{-1}·h^{-1}, 9.5% CO content) and $Ni_{NP}/La_2O_2CO_3$ (221 mmol·g^{-1}·h^{-1}, 4.3% CO content). Theoretical calculations indicate that the coupling of Ni single atoms and Ni nanoparticles can reduce the C–C bond and C–H bond cleavage energy barriers form 1.48 and 1.09 to 0.88 and 0.65 eV, respectively, thus

promoting the dissociation of ethanol and strengthen the CO adsorption to reduce the CO concentration in hydrogen gas. As a result, the $Ni_{SA+NP}/La_2O_2CO_3$ combined with the self-made photothermal reactor shows the 1129 mmol·g^{-1}·h^{-1} of H_2 production rate, 0.4% CO content and 16.6% STH efficiency under 1.3 suns irradiation, superior to current reports. This work provides a promising strategy for the efficient and low-energy decomposition of fermentation broth to produce high quality H_2 using natural sunlight, laying one of the foundations for future hydrogen energy systems.

Electronic Supplementary Material: Supplementary material (experimental details and supplementary figures and tables) is available in the online version of this article at https://doi.org/10.26599/NR.2026.94908665.

Data availability

All data needed to support the conclusions in the paper are presented in the manuscript and the Electronic Supplementary Material. Additional data related to this paper may be requested from the corresponding author upon request.

Acknowledgements

This work was supported by the National Natural Science Foundation of China (Nos. 52371220 and U23A20139), Scientific Research Innovation Capability Support Project for Young Faculty, and Hebei Natural Science Foundation (Nos. B2023204034, B2023201107, and 2023HBQZYCXY001).

Declaration of competing interest

All the contributing authors report no conflict of interests in this work.

Author contribution statement

J. Q. P.: Investigation, formal analysis, writing – original draft. Y. Y. S.: Formal analysis, validation. T. C. C.: Investigation. D. C. Y.: Methodology, writing – original draft. G. D. H.: Data curation. L. P. M.: Validation. S. H. Y.: Resource. Y. G. L.: Supervision, funding acquisition, methodology, writing – review & editing. J. H. Y.: Supervision, project administration, funding acquisition, writing – review & editing. All the authors have approved the final manuscript.

Use of AI statement

None.

References

[1] Keller, N.; Ivanez, J.; Highfield, J.; Ruppert, A. M. Photo-/thermal synergies in heterogeneous catalysis: Towards low-temperature (solar-driven) processing for sustainable energy and chemicals. *Appl. Catal. B: Environ.* **2021**, *296*, 120320.

[2] Pan, H.; Li, J. L.; Wang, Y. G.; Xia, Q. N.; Qiu, L.; Zhou, B. W. Solar-driven biomass reforming for hydrogen generation: Principles, advances, and challenges. *Adv. Sci.* **2024**, *11*, 2402651.

[3] Sanchez, N.; Ruiz, R.; Hacker, V.; Cobo, M. Impact of bioethanol impurities on steam reforming for hydrogen production: A review. *Int. J. Hydrogen Energy* **2020**, *45*, 11923–11942.

[4] Zhang, P.; Guo, Y. J.; Chen, J. B.; Zhao, Y. R.; Chang, J.; Junge, H.; Beller, M.; Li, Y. Streamlined hydrogen production from biomass. *Nat. Catal.* **2018**, *1*, 332–338.

[5] Pandiyan, K.; Singh, A.; Singh, S.; Saxena, A. K.; Nain, L. Technological interventions for utilization of crop residues and weedy biomass for second generation bio-ethanol production. *Renew. Energy* **2019**, *132*, 723–741.

[6] Sanchez, N.; Ruiz, R. Y.; Cifuentes, B.; Cobo, M. Controlling sugarcane press-mud fermentation to increase bioethanol steam reforming for hydrogen production. *Waste Manage.* **2019**, *98*, 1–13.

[7] Zheng, Y. H.; Wang, Y. X.; Li, R. T.; Yang, H. R.; Dai, Y. Y.; Niu, Q.; Lin, T. J.; Gong, K.; Zhong, L. S. CO_2-free hydrogen production from solar-driven photothermal catalytic decomposition of methane. *Chin. J. Catal.* **2025**, *73*, 289–299.

[8] Yuan, D. C.; Peng, Y. H.; Ma, L. P.; Li, J. C.; Zhao, J. G.; Hao, J. J.; Wang, S. F.; Liang, B. L.; Ye, J. H.; Li, Y. G. Coke and sintering resistant nickel atomically doped with ceria nanosheets for highly efficient solar driven hydrogen production from bioethanol. *Green Chem.* **2022**, *24*, 2044–2050.

[9] Yuan, D. C.; Han, G. D.; Wang, Z. X.; Zhao, J. G.; Li, K. L.; Wang, P. F.; Hao, J. J.; Li, Y. G.; Ye, J. H. Hybrid structure of iron single atoms and metallic titanium for photothermal ethanol steam reforming. *Sci. China Chem.* **2024**, *67*, 848–854.

[10] Zhong, B. L.; Hu, J. D.; Yang, X. G.; Shu, Y. Y.; Cai, Y. H.; Li, C. M.; Qu, J. F. Metal species confined in metal-organic frameworks for CO_2 hydrogenation: Synthesis, catalytic mechanisms, and future perspectives. *Chin. J. Catal.* **2025**, *68*, 177–203.

[11] Chen, F. Y.; Tao, Y. W.; Ling, H. J.; Zhou, C. F.; Liu, Z. W.; Huang, J.; Yu, A. B. Ni–Cu bimetallic catalysts on Yttria-stabilized zirconia for hydrogen production from ethanol steam reforming. *Fuel* **2020**, *280*, 118612.

[12] Shi, W. Z.; Zhang, R. J.; Li, H. W.; Wu, Y.; Sun, Z.; Sun, Z. Q. Constructing MAX-derived atomically dispersed Ni-based catalysts for efficient bioethanol steam reforming. *Int. J. Hydrogen Energy* **2025**, *126*, 200–209.

[13] Wang, M. Y.; Kim, S. Y.; Jamsaz, A.; Pham-Ngoc, N.; Men, Y.; Jeong, D. H.; Shin, E. W. Effect of active sites distributions on temperature dependent-coke formation over $Ni/Ce_xZr_{1-x}O_2$–Al_2O_3 catalysts for ethanol steam reforming: Coke precursor gasification. *Appl. Surf. Sci.* **2024**, *644*, 158746.

[14] Musso, M.; Cardozo, A.; Romero, M.; Faccio, R.; Segobia, D.; Apesteguía, C.; Bussi, J. High performance Ni-catalysts supported on rare-earth zirconates (La and Y) for hydrogen production through ethanol steam reforming. Characterization and assay. *Catal. Today* **2022**, *394–396*, 524–538.

[15] Hou, Y. H.; Han, W. C.; Xia, W. S.; Wan, H. L. Structure sensitivity of $La_2O_2CO_3$ catalysts in the oxidative coupling of methane. *ACS Catal.* **2015**, *5*, 1663–1674.

[16] Li, X. Y.; Li, D.; Tian, H.; Zeng, L.; Zhao, Z. J.; Gong, J. L. Dry reforming of methane over Ni/La_2O_3 nanorod catalysts with stabilized Ni nanoparticles. *Appl. Catal. B: Environ.* **2017**, *202*, 683–694.

[17] Ding, T.; Liu, X. K.; Tao, Z. N.; Liu, T. Y.; Chen, T.; Zhang, W.; Shen, X. Y.; Liu, D.; Wang, S. C.; Pang, B. B. et al. Atomically precise dinuclear site active toward electrocatalytic CO_2 reduction. *J. Am. Chem. Soc.* **2021**, *143*, 11317–11324.

[18] Hou, M. Y.; Zheng, L. R.; Zhao, D.; Tan, X.; Feng, W. Y.; Fu, J. T.; Wei, T. X.; Cao, M. H.; Zhang, J. T.; Chen, C. Microenvironment reconstitution of highly active Ni single atoms on oxygen-incorporated Mo_2C for water splitting. *Nat. Commun.* **2024**, *15*, 1342.

[19] Shen, W. J. Ionic exchange of metal-organic frameworks to access single nickel sites for efficient electroreduction of CO_2. *Acta Phys. Chim. Sin.* **2018**, *34*, 113–114.

[20] Faroldi, B. M.; Múnera, J. F.; Cornaglia, L. M. *In situ* characterization of phase transformation and reactivity of high surface area lanthanum-based Ru catalysts for the combined reforming of methane. *Appl.*

Catal. B: Environ. **2014**, *150–151*, 126–137.
[21] Shen, Y.; Lua, A. C. Polyol synthesis of nickel-copper based catalysts for hydrogen production by methane decomposition. *Int. J. Hydrogen Energy* **2015**, *40*, 311–321.
[22] Zhao, Y.; Wang, T. H.; Wang, X. H.; Hao, R. L.; Wang, H. CO_2 hydrogenation to formate over nano-scale zero-valent nickel catalyst under atmospheric pressure. *Chem. Eng. J.* **2018**, *347*, 860–869.
[23] Vizcaíno, A. J.; Carrero, A.; Calles, J. A. Hydrogen production by ethanol steam reforming over Cu–Ni supported catalysts. *Int. J. Hydrogen Energy* **2007**, *32*, 1450–1461.
[24] Xu, W. Q.; Liu, Z. Y.; Johnston-Peck, A. C.; Senanayake, S. D.; Zhou, G.; Stacchiola, D.; Stach, E. A.; Rodriguez, J. A. Steam reforming of ethanol on Ni/CeO_2: Reaction pathway and interaction between Ni and the CeO_2 support. *ACS Catal.* **2013**, *3*, 975–984.
[25] Peng, M.; Ge, Y. Z.; Gao, R.; Yang, J.; Li, A. W.; Xie, Z. H.; Yu, Q. L.; Zhang, J.; Asakura, H.; Zhang, H. et al. Thermal catalytic reforming for hydrogen production with zero CO_2 emission. *Science* **2025**, *387*, 769–775.
[26] Li, Y. G.; Bai, X. H.; Yuan, D. C.; Zhang, F. Y.; Li, B.; San, X. Y.; Liang, B. L.; Wang, S. F.; Luo, J.; Fu, G. S. General heterostructure strategy of photothermal materials for scalable solar-heating hydrogen production without the consumption of artificial energy. *Nat. Commun.* **2022**, *13*, 776.
[27] Li, Y. G.; Guan, Q. Q.; Huang, G. Y.; Yuan, D. C.; Xie, F.; Li, K. L.; Zhang, Z. B.; San, X. Y.; Ye, J. H. Low temperature thermal and solar heating carbon-free hydrogen production from ammonia using nickel single atom catalysts. *Adv. Energy Mater.* **2022**, *12*, 2202459.
[28] Luo, S. Q.; Song, H.; Philo, D.; Oshikiri, M.; Kako, T.; Ye, J. H. Solar-driven production of hydrogen and acetaldehyde from ethanol on Ni–Cu bimetallic catalysts with solar-to-fuels conversion efficiency up to 3.8 %. *Appl. Catal. B: Environ.* **2020**, *272*, 118965.
[29] Zhou, P.; Zhang, Q. H.; Chao, Y. G.; Wang, L.; Li, Y. J.; Chen, H.; Gu, L.; Guo, S. J. Partially reduced Pd single atoms on CdS nanorods enable photocatalytic reforming of ethanol into high value-added multicarbon compound. *Chem* **2021**, *7*, 1033–1049.
[30] Davis, K. A.; Yoo, S.; Shuler, E. W.; Sherman, B. D.; Lee, S.; Leem, G. Photocatalytic hydrogen evolution from biomass conversion. *Nano Converg.* **2021**, *8*, 6.
[31] Song, H.; Luo, S. Q.; Huang, H. M.; Deng, B. W.; Ye, J. H. Solar-driven hydrogen production: Recent advances, challenges, and future perspectives. *ACS Energy Lett.* **2022**, *7*, 1043–1065.
[32] Young, J. L.; Steiner, M. A.; Döscher, H.; France, R. M.; Turner, J. A.; Deutsch, T. G. Direct solar-to-hydrogen conversion via inverted metamorphic multi-junction semiconductor architectures. *Nat. Energy* **2017**, *2*, 17028.
[33] Zhou, P.; Navid, I. A.; Ma, Y. J.; Xiao, Y. X.; Wang, P.; Ye, Z. W.; Zhou, B. W.; Sun, K.; Mi, Z. T. Solar-to-hydrogen efficiency of more than 9% in photocatalytic water splitting. *Nature* **2023**, *613*, 66–70.